CANCER

Tracking extracellular vesicle phenotypic changes enables treatment monitoring in melanoma

Jing Wang[1]*, Alain Wuethrich[1]*, Abu Ali Ibn Sina[1], Rebecca E. Lane[1], Lynlee L. Lin[1,2], Yuling Wang[3]†, Jonathan Cebon[4,5], Andreas Behren[4,5], Matt Trau[1,6]†

Monitoring targeted therapy in real time for cancer patients could provide vital information about the development of drug resistance and improve therapeutic outcomes. Extracellular vesicles (EVs) have recently emerged as a promising cancer biomarker, and EV phenotyping shows high potential for monitoring treatment responses. Here, we demonstrate the feasibility of monitoring patient treatment responses based on the plasma EV phenotypic evolution using a multiplex EV phenotype analyzer chip (EPAC). EPAC incorporates the nanomixing-enhanced microchip and the multiplex surface-enhanced Raman scattering (SERS) nanotag system for direct EV phenotyping without EV enrichment. In a preclinical model, we observe the EV phenotypic heterogeneity and different phenotypic responses to the treatment. Furthermore, we successfully detect cancer-specific EV phenotypes from melanoma patient plasma. We longitudinally monitor the EV phenotypic evolution of eight melanoma patients receiving targeted therapy and find specific EV profiles involved in the development of drug resistance, reflecting the potential of EV phenotyping for monitoring treatment responses.

INTRODUCTION

Targeted therapies can slow down the progress of many cancers by disrupting molecular activities of targeted cellular pathways and mutated genes, which, in turn, blocks the outgrowth of tumor cells (*1*). Although targeted therapies are effective, most patients develop a drug nonresponsiveness within months, which eventually results in tumor relapse (*1*). A promising way to improve therapeutic outcomes could be the use of informative biomarkers and technologies to track therapy responses in real time and predict the early development of drug resistance with the aim of treatment adjustment (*2*). In this context, extracellular vesicles (EVs) have emerged as informative biomarkers with high potential to become an important tool for cancer diagnosis and therapy monitoring (*3*, *4*). EVs are membrane-encapsulated nanoscopic bodies that are secreted from cells (*3*). EVs carry functional molecular cargoes that include transmembrane/cytoplasmic proteins, DNAs/RNAs, and lipids, which serve as biomarkers for tumor staging and predicting responses to therapy (*5*). For instance, by characterizing EV phenotypes (defined by the relative levels of transmembrane proteins), recent studies have successfully obtained proteomic information to forecast the metastatic stages in glioma (*6*) and melanoma (*7*). In addition, tracking of treatment responses via EV phenotypes has been demonstrated in glioblastoma (*8*, *9*), breast carcinoma (*10*, *11*), pancreatic cancer (*12*), and colorectal cancer (*13*). In the case of colorectal cancer, the EV phenotype served as an indication for successful surgical removal of the tumor by a decreased level of a double-positive CD147/CD9 EV subpopulation (*13*).

While there is growing evidence suggesting that EV phenotypes reflect biological functions including metastasis and therapy resistance (*5*), the clinical translation of EVs is limited by the EV heterogeneity. The EV heterogeneity makes it extremely difficult to isolate and detect specific EV subpopulations (e.g., tumor-derived EVs) among other nontarget EVs present in circulation. For example, different EV subpopulations can have similar morphological and physical properties (e.g., size), which can result in co-isolation of bulk EV populations and render the interrogation of target EV subpopulations intractable (*5*). In addition, multiplex phenotyping of EVs in a small volume for treatment monitoring is also impractical to be achieved with conventional methods such as immunoblotting and enzyme-linked immunosorbent assay (ELISA). Recently, there are a few new technologies that have been developed for the multiplex EV phenotype analysis; however, most of them are not a real multiplex assay, as these methods do not measure multiple biomarkers simultaneously (*8*, *14*, *15*). These methods have not been used to perform longitudinal studies to better understand EV phenotypic evolution in response to treatment. Here, we develop an EV phenotype analyzer chip (EPAC) for EV phenotype analysis to enable the monitoring of therapy responses over time. EPAC uses a nanomixing strategy to minimize the nonspecific adsorption, which is particularly beneficial when capturing EVs directly from complex biological samples. This is followed by a multiplex phenotype readout using surface-enhanced Raman spectroscopy (SERS). We achieve multiplex biomarker detection by simultaneously labeling the target EVs with unique SERS nanotags [i.e., gold nanoparticles (AuNPs) with dedicated reporters and tumor-specific antibodies].

Using EPAC, we monitor the EV phenotypic changes in four patient-derived melanoma cell lines treated with the BRAF inhibitor that targets mutant BRAF V600, which is found in approximately 40% of melanoma patients (*16*). We focus on the detection of four selected biomarkers in EVs including melanoma chondroitin sulfate proteoglycan (MCSP), melanoma cell adhesion molecule (MCAM), low-affinity nerve growth factor receptor (LNGFR), and receptor tyrosine protein kinase (ErbB3). These biomarkers have been demonstrated to often change with treatment and melanoma progression

[1]Centre for Personalized Nanomedicine, Australian Institute for Bioengineering and Nanotechnology (AIBN), The University of Queensland, Brisbane, QLD 4072, Australia. [2]Dermatology Research Centre, University of Queensland Diamantina Institute, The University of Queensland, Brisbane, QLD 4102, Australia. [3]Department of Molecular Sciences, ARC Centre of Excellence for Nanoscale BioPhotonics, Faculty of Science and Engineering, Macquarie University, Sydney, NSW 2109, Australia. [4]Olivia Newton-John Cancer Research Institute, School of Cancer Medicine, La Trobe University, Heidelberg, VIC 3084, Australia. [5]Department of Medicine, University of Melbourne, Heidelberg, VIC 3084, Australia. [6]School of Chemistry and Molecular Biosciences, The University of Queensland, Brisbane, QLD 4072, Australia.
*These authors contributed equally to this work.
†Corresponding author. Email: yuling.wang@mq.edu.au (Y.W.); m.trau@uq.edu.au (M.T.)

(17). We monitor and observe EV heterogeneity and phenotype variations based on changes in the expression levels of these four biomarkers during the treatment. EPAC further enables the differentiation of 11 melanoma patients and 12 healthy individuals based on plasma EV phenotypes, as well as the monitoring of phenotypic changes in EVs from 8 melanoma patients receiving targeted therapies.

RESULTS AND DISCUSSION
Working scheme
The schematic workflow of EPAC for monitoring the EV phenotypic evolution during treatment is shown in Fig. 1. As indicated in Fig. 1A, we selected melanoma cell–derived EVs as a model whose parental cell lines harbor the BRAF V600E mutation to evaluate

responses to the BRAF inhibitor treatment. The BRAF V600E mutation leads to constitutive activation of the cellular mitogen-activated protein kinase (MAPK) signaling pathway (Fig. 1A), thereby driving cell cycle progression and tumor growth (18). Treating BRAF V600 mutant melanoma patients or cell lines with BRAF inhibitors specifically disrupts this pathway to shrink or slow tumor growth (18). As the molecular information packaged within EVs originates directly from their parental tumor cells, we speculated that profiling melanoma EV phenotypes might provide a snapshot of the host cell state, making it feasible to be implemented as a treatment monitoring biomarker.

To analyze the phenotypes of melanoma EVs directly from complex biological samples (i.e., cell culture medium and diluted patient plasma) without the need for purification and enrichment
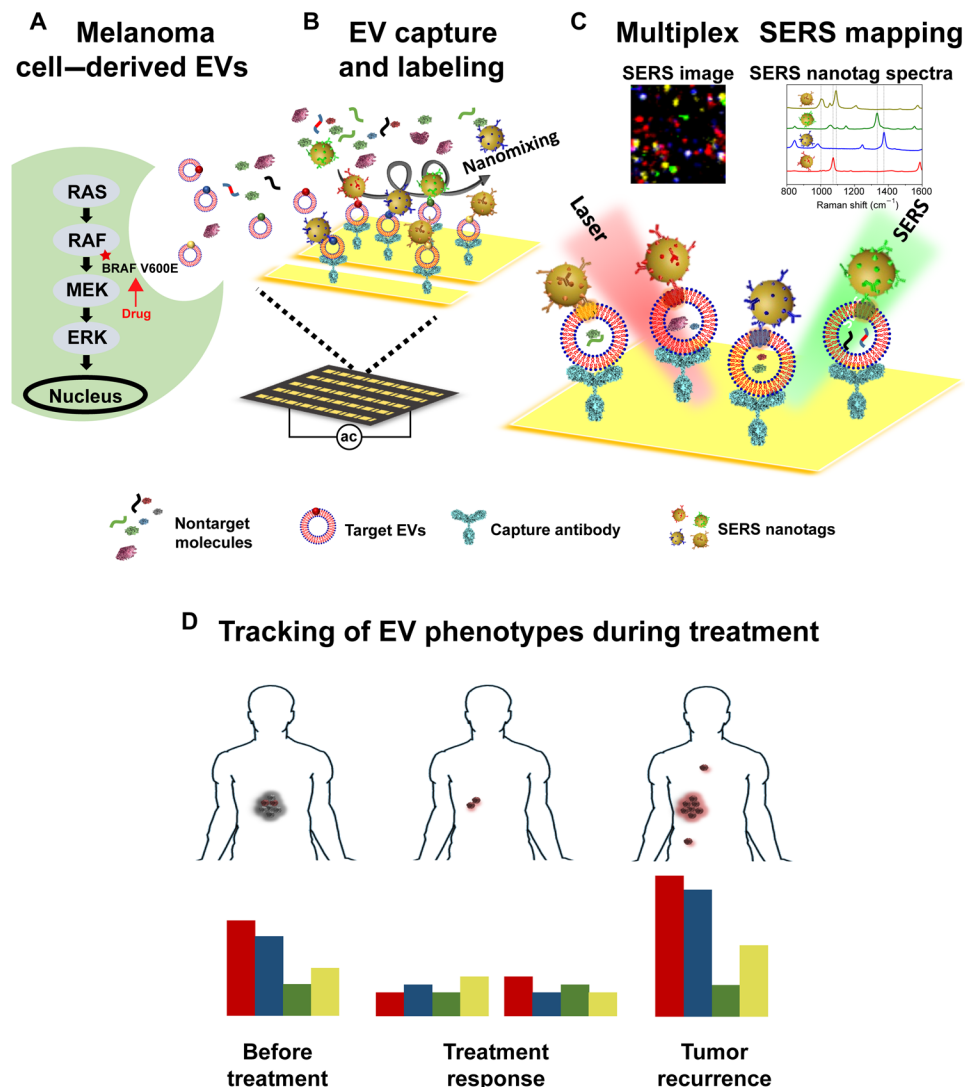
Fig. 1. Schematic for EV phenotyping by EPAC. (**A**) A melanoma cell with a BRAF V600E mutation secretes EVs into circulation or cell culture medium. (**B**) The sample is directly injected into EPAC, where the applied nanomixing fluid flow increases EV collisions with the capture antibody and SERS nanotags and shears off nontarget molecules (e.g., protein aggregates and apoptotic bodies) and free SERS nanotags. (**C**) The characterization of EV phenotypes is performed by SERS mapping. The false-color SERS spectral images are established on the basis of the characteristic peak intensities of SERS nanotags (MCSP-MBA, red; MCAM-TFMBA, blue; ErbB3-DTNB, green; LNG-FR-MPY, yellow). (**D**) EV phenotypes defined by the relative expression levels of four biomarkers are extracted from the average signal spectra of false-color SERS spectral images. EV phenotypes are unique to each EV subpopulation. By analyzing EV samples before, during, and after BRAF inhibitor treatment, the phenotypic evolution can be tracked to provide information on treatment responses and early signs of drug resistance.

steps, we performed the immunoaffinity-based isolation and labeling via the EPAC (Fig. 1B). To characterize the EVs using EPAC, we used a nanomixing strategy developed in our laboratory (see Materials and Methods) (19, 20). The EPAC not only improved the EV capture efficiency as indicated previously (20) but also addressed the critical problems present in current EV SERS phenotyping technologies, such as nonspecific adsorption and long incubation time because of slow binding kinetics of SERS nanotags to target EVs. The nanomixing force thereby enabled a streamlined plasma EV phenotype analysis within 40 min, which was faster than conventional methods [e.g., >3 hours given by >1 hour for EV isolation (21) and >2 hours for ELISAs (22)]. The stepwise functionalization of EPAC is shown in fig. S1.

To profile EV phenotypes in a small sample volume, EPAC relies on a multiplex SERS nanotag system (Fig. 1C). Each type of SERS nanotags targeted a single biomarker: 4-mercaptobenzoic acid (MBA) for MCSP, 2,3,5,6-tetrafluoro-MBA (TFMBA) for MCAM, 5,5′-dithiobis (2-nitrobenzoic acid) (DTNB) for ErbB3, and 4-mercaptopyridine (MPY) for LNGFR. The signal readout was achieved by SERS mapping. The false-color SERS spectral image was generated on the basis of the characteristic peaks of Raman reporters ($1075\ cm^{-1}$ for MBA, $1375\ cm^{-1}$ for TFMBA, $1335\ cm^{-1}$ for DTNB, and $1000\ cm^{-1}$ for MPY). The signal intensities in the mapped area were proportional to the numbers of EVs and their expressing biomarker levels.

The EPAC was then applied for the characterization of EV phenotypes before, during, and after treatment (Fig. 1D). The EV phenotypes were obtained from false-color SERS spectral images by calculating the relative intensities of Raman reporter peaks. We hypothesized that the overall EV phenotypic changes could reflect changes in cancer cell populations during treatment and could thus be useful for monitoring of patient treatment responses.

EPAC characterization

To demonstrate the capture capability of EPAC, we characterized SK-MEL-28 cell–derived EVs before and after being captured by EPAC. Nanoparticle tracking analysis (NTA) was used to determine the size distribution of particles (including EVs) present in the conditioned culture medium of SK-MEL-28, showing a mean particle diameter of 148.9 nm and a modal diameter of 102.3 nm (fig. S2A). Atomic force microscopy (AFM) measurements were then applied to in situ characterize SK-MEL-28 cell–derived EVs captured by EPAC (fig. S2, B and C). To capture CD63-positive EVs from the conditioned culture medium, we functionalized EPAC with anti-CD63 antibodies (fig. S2B). We further tested the capture of EVs from simulated patient plasma (i.e., pooled plasma from healthy donors spiked with the same concentration of SK-MEL-28 cell–derived EVs) using the anti-MCSP antibody functionalized EPAC (fig. S2C). The anti-MCSP antibody functionalized EPAC was designed for clinical sample detection, as melanoma-derived EVs are found at low concentrations (less than 1% of total plasma EVs) (23), and MCSP is highly expressed in melanoma cells (24). The anti-MCSP functionalized EPAC exposed to normal plasma (fig. S2D) and the anti-MCSP functionalized EPAC (fig. S2E) were used as controls to provide an indication of background signals. Compared to the controls (fig. S2, D and E), both two-dimensional (2D) and 3D AFM images indicated that anti-CD63 and anti-MCSP antibody functionalized EPAC captured particles (i.e., EVs) from the conditioned culture medium and the simulated patient plasma, respectively (fig. S2, B and C). The diameters of two representative particles in each group ranged from

155 to 277 nm, which was in line with the diameter distribution of EVs measured by NTA data (fig. S2A) and thus suggested the successful capture of EVs by EPAC.

To further evaluate the performance of anti-CD63 and anti-MCSP functionalized EPACs in sensing melanoma-specific EVs, we applied these two types of EPACs to detect MCSP-positive EVs present in the conditioned culture medium of SK-MEL-28 cells. To avoid the binding of anti-MCSP capture and detection antibodies toward the same epitope binding site of MCSP, we used antibodies from two different monoclonal clones. We observed a stronger MCSP SERS signal from the anti-MCSP functionalized EPAC than the anti-CD63 functionalized EPAC (Fig. 3D and fig. S7C), possibly due to a higher level of MCSP expression than CD63 in MCSP-positive EVs derived from SK-MEL-28 cells and/or a stronger binding affinity of the MCSP antibody than the anti-CD63 antibody. Hence, we applied the anti-MCSP functionalized EPAC for detection of melanoma-specific EVs derived from patient plasma.

To explore the sensitivity of EPAC in detecting MCSP-positive EVs, we captured different numbers of EVs released from SK-MEL-28 cells in conditioned culture medium and simulated patient plasma samples by the anti-CD63 (Fig. 2A) and anti-MCSP (Fig. 2B) functionalized EPACs, respectively, followed by the labeling of MCSP-MBA SERS nanotags. As shown in Fig. 2, there were statistically significant differences between each of these dilutions [one-way analysis of variance (ANOVA), $P < 0.05$]. According to the signal-to-noise ratio > 3 (the noise signal was measured from medium/plasma only), the anti-CD63 functionalized EPAC was able to detect 10^8 EVs/ml from the conditioned culture medium (Fig. 2A), while the anti-MCSP functionalized EPAC could detect as low as 10^5 EVs/ml in the simulated patient plasma (Fig. 2B). The detection sensitivity of the anti-MCSP functionalized EPAC meets the clinical requirement, given that the average melanoma EV concentration in plasma is ~10^6 EVs/ml (23, 25). Both resulting sensitivities are also comparable to or better than other EV detection technologies such as the miniaturized EV capture device developed by Kwizera and co-workers (14), although direct comparisons are difficult due to differences in capture/detection antibodies and sample sources.

To demonstrate the detection specificity of EPAC, we measured EVs derived from two cell lines (melanoma SK-MEL-28 and breast cancer MCF7) with known differences in biomarker expression levels (17), together with control experiments (i) EV-free cell culture medium, (ii) without the CD63 capture antibody, and (iii) with nontarget CD45 detection antibodies on SERS nanotags. According to previous reports (26–31), SK-MEL-28 cells show high expressions of MCSP and MCAM and low expressions of ErbB3 and LNGFR; MCF7 cells have low expressions of all four biomarkers. We also performed flow cytometry to validate these four biomarker expressions in SK-MEL-28 and MCF7 cell lines before performing their EV characterization (Fig. 3A). As shown in Fig. 3 (B to D), SK-MEL-28 cell–derived EVs provided a unique signal profile compared to MCF7 cell–derived EVs—with the SERS intensity order of MCSP > MCAM > LNGFR > ErbB3—according to the representative false-color SERS spectral images, average SERS spectra obtained from corresponding SERS imaging datasets, and average SERS intensities at 1075, 1375, 1335, and $1000\ cm^{-1}$ from three replicates. Only negligible nonspecific signals were observed from the MCF7 cell–derived EVs and other control experiments. The unique phenotypes of SK-MEL-28 cell–derived EVs and the negligible backgrounds from controls indicated that EPAC was capable of performing multiplex
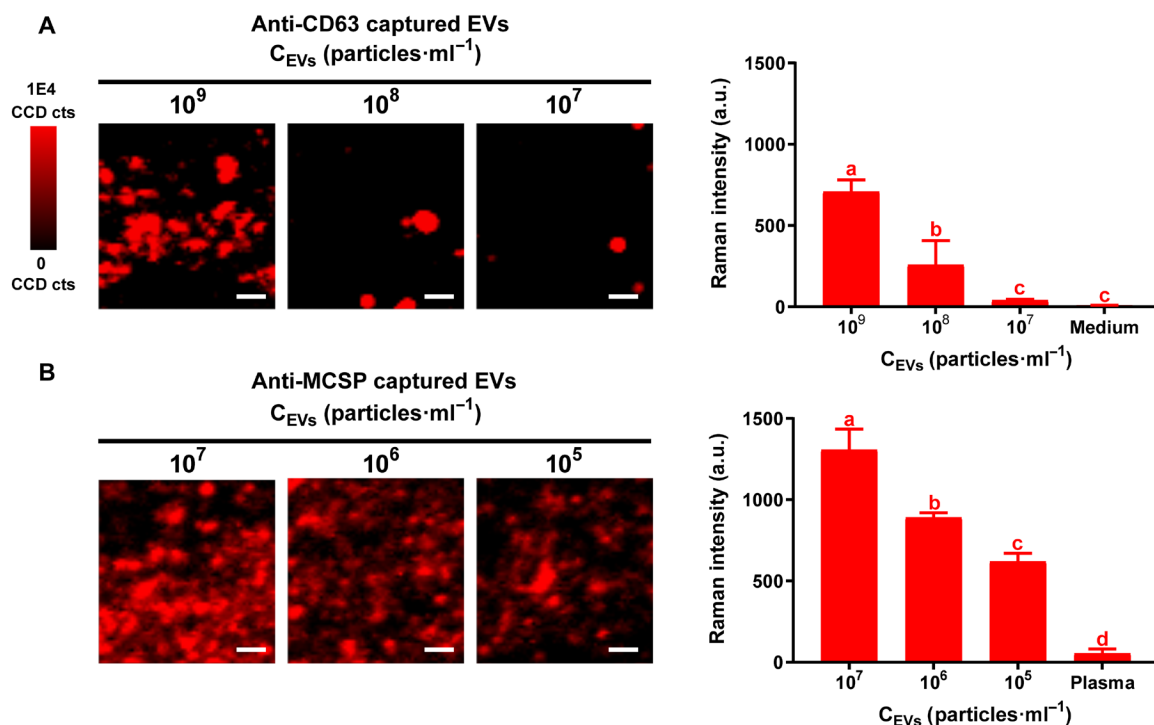
Fig. 2. EPAC sensitivity. The EPAC sensitivity was studied by analyzing designated concentrations of SK-MEL-28 cell–derived EVs from (**A**) the conditioned culture medium using an anti-CD63 functionalized EPAC and (**B**) the simulated patient plasma using an anti-MCSP functionalized EPAC, followed by labeling with MCSP-MBA SERS nanotags. The left side shows the representative false-color SERS spectral images, and the right side is the concentration-dependent average SERS intensity at 1075 cm^{-1}. Data are represented as means ± standard deviation, where error bars represent standard deviation of three separate experiments. Means not sharing a common letter are significantly different ($P < 0.05$). Scale bars, 10 μm. a.u., arbitrary units.

EV phenotype characterization and accurately recognizing different EV subpopulations. We believe that our method would be valuable for the study of EV biogenesis, tumor heterogeneity, tumor staging, and phenotypic changes concomitantly during treatment.

To further validate EPAC results, we then measured the expressions of MCSP, MCAM, ErbB3, and LNGFR biomarkers in EVs derived from SK-MEL-28 and MCF7 cell lines using Western blot (fig. S3). As indicated in fig. S3, SK-MEL-28 cell–derived EVs showed MCSP, MCAM, and LNGFR signals and negligible ErbB3 signals; MCF7 cell–derived EVs indicated negative signals for all four biomarkers. These Western blot results were in line with EPAC results and confirmed the presence of MCSP, MCAM, and LNGFR in SK-MEL-28 cell–derived EVs and the low abundance of all four biomarkers in MCF7 cell–derived EVs (Fig. 3B).

Monitoring the EV phenotypic evolution during treatment in preclinical models

Detecting the emergence of drug resistance and identifying potential resistance mechanisms are clinically important for personalized therapy management. To understand the effect of drug treatment on the expression of tumor-specific biomarkers in EVs, we strategically selected generic EV biomarkers as the capture antibody instead of melanoma-associated MCSP. We then investigated the capture efficiency of using three tetraspanin EV biomarkers (i.e., CD63, CD9, and CD81) for detecting MCSP-positive EVs derived from SK-MEL-28. The captured EVs were recognized using MCSP-MBA SERS nanotags. The false-color SERS spectral images derived from anti-CD63/CD9/CD81 functionalized EPACs (fig. S4A) were estab-

lished on the basis of the characteristic peak of MBA at 1075 cm^{-1}. We then selected CD63 as the biomarker for EV capture because the anti-CD63 functionalized EPAC provided the highest signal density in SERS mapping data (fig. S4A), corresponding average SERS spectral signals from the SERS mapping data (fig. S4B), and average SERS intensities at 1075 cm^{-1} from triplicate measurements (fig. S4C). This result might be due to (i) a higher level of CD63 expression than those of CD9/CD81 in SK-MEL-28 cell–derived EVs and (ii) a stronger binding affinity of the anti-CD63 antibody than anti-CD9/CD81 antibodies. These possibilities, however, are extremely difficult to validate by antibody-based methods, given the different binding affinities for each antibody.

To investigate whether and how the phenotypes of CD63-positive EVs change during treatment, we characterized EVs from four patient-derived melanoma cell lines harboring either a BRAF mutation (LM-MEL-33, LM-MEL-64, and SK-MEL-28) or an NRAS mutation in a BRAF wild type setting as a control (LM-MEL-35) (*32*). We first characterized the EV phenotype before drug treatment (Fig. 4, day 0). MCSP that is expressed in more than 85% of primary and metastatic melanoma lesions (*33*) was highly expressed in EVs from all four melanoma cell lines. MCAM, cell adhesion–associated surface protein potentially implicated in metastatic spread (*27*), showed higher expression in LM-MEL-33 cell–derived EVs than in the other studied EVs. Together, EPAC provided a unique phenotypic snapshot that reflected cell type–specific fingerprints (e.g., overexpressed proteins).
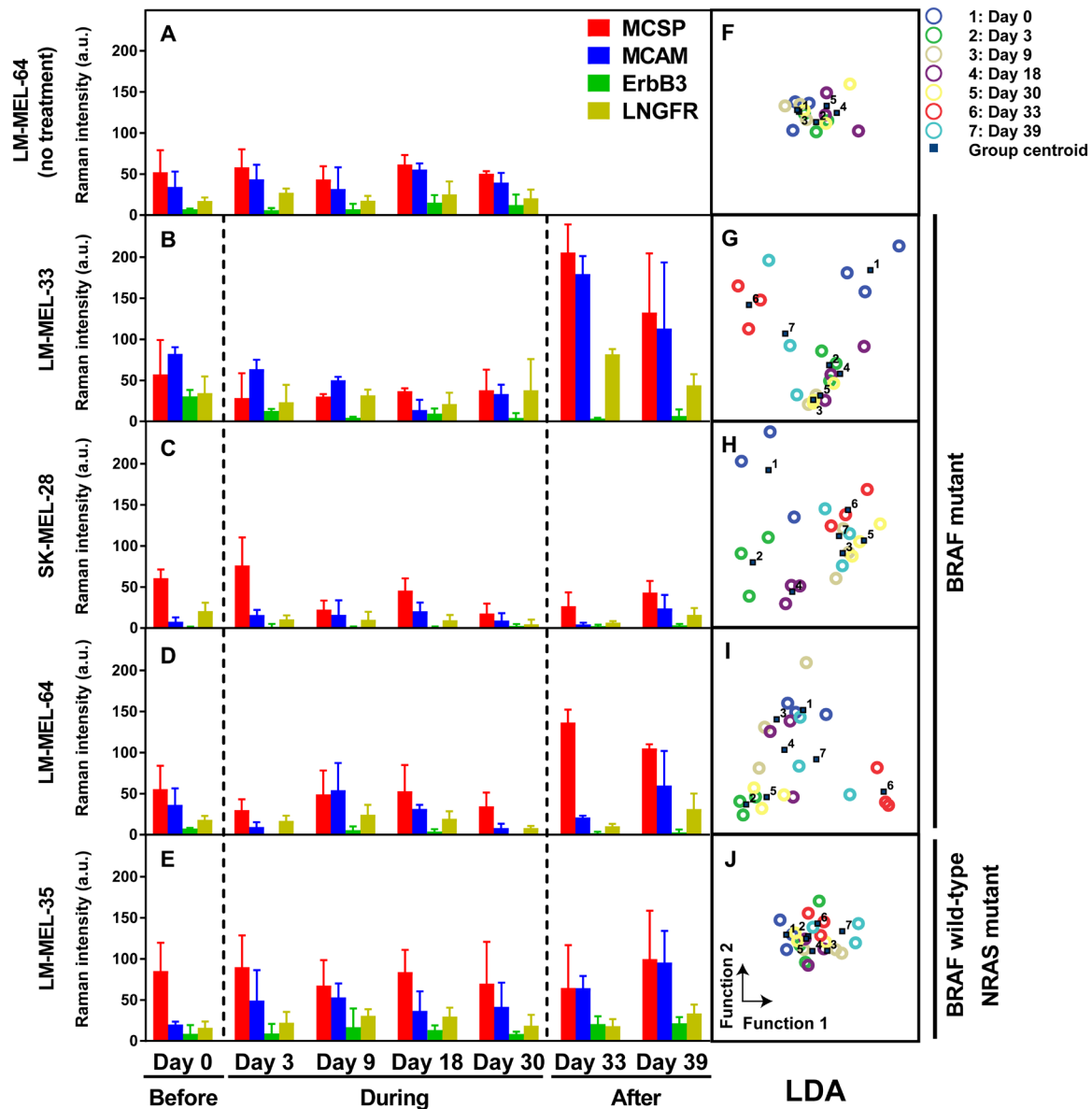
To monitor treatment responses of melanoma cell lines, we characterized their EV phenotypic evolution (Fig. 4) and performed
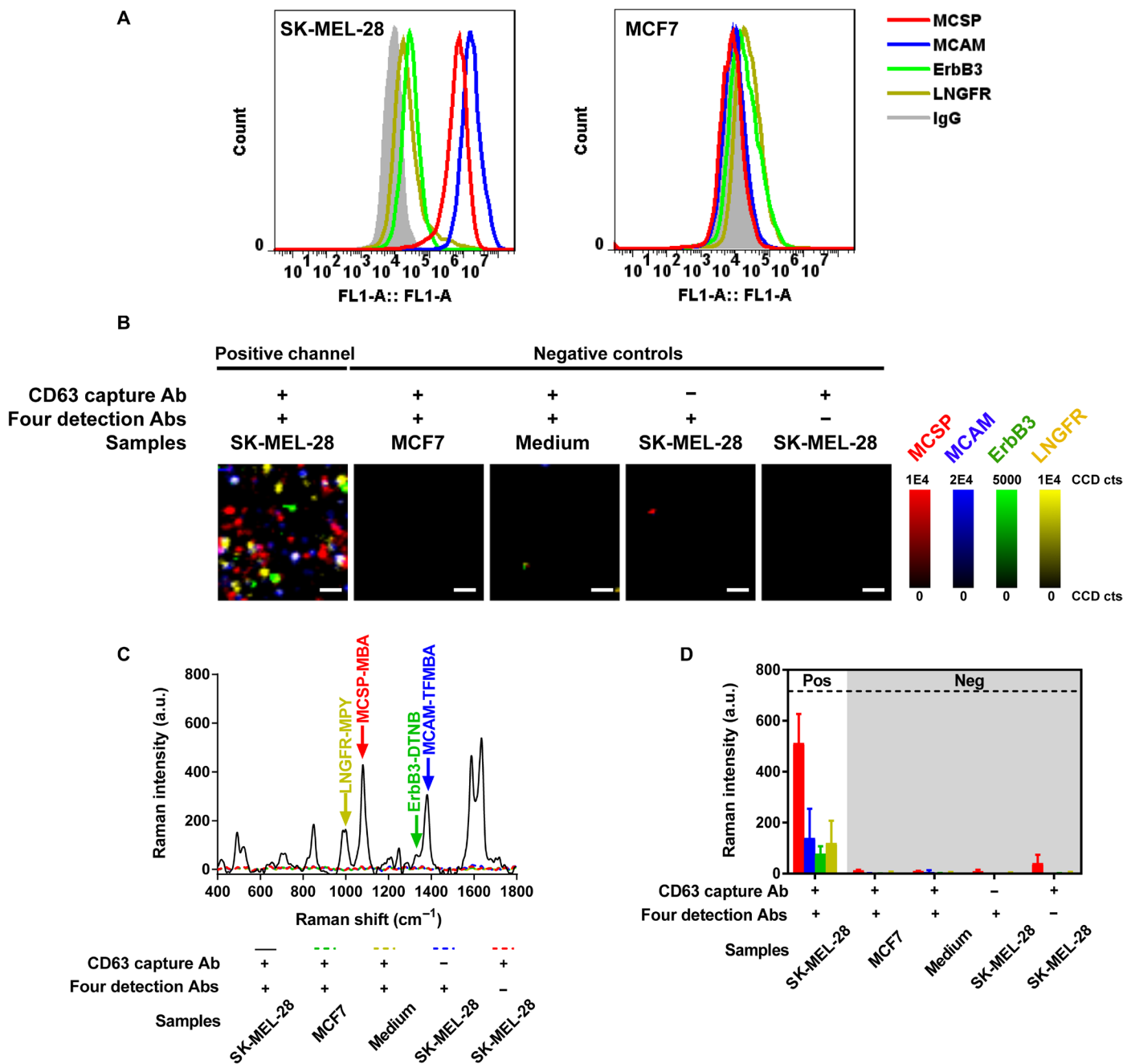
Fig. 3. Anti-CD63 functionalized EPAC specificity. The specificity was studied using EV samples released from SK-MEL-28 and MCF7 cell lines, as well as control experiments including (++) EV-free cell culture medium, (−+) without the CD63 capture antibody, and (+−) with nontarget CD45 detection antibodies on SERS nanotags. (**A**) The expressions of MCSP, MCAM, ErbB3, and LNGFR in SK-MEL-28 and MCF7 cells were detected by flow cytometry. (**B**) Representative false-color SERS spectral images, (**C**) average SERS spectra obtained from corresponding SERS mapping datasets, and (**D**) average SERS intensities at 1075 cm^{-1} (red, MCSP), 1375 cm^{-1} (blue, MCAM), 1335 cm^{-1} (green, ErbB3), and 1000 cm^{-1} (yellow, LNGFR). Data in (D) are represented as means ± standard deviation, where error bars represent standard deviation of three separate experiments. Scale bars, 10 μm.

one-way ANOVA to statistically evaluate the changes of each bio-marker (fig. S5) during 30 days of drug treatment and 9 days after treatment. LM-MEL-64 cells without drug treatment were used as a control, which showed no obvious EV phenotypic changes across four selected biomarkers over the same period ($P > 0.05$), suggesting negligible effects from cell passaging artifacts (fig. S5). With the initiation of drug treatment, BRAF inhibitors affect BRAF mutant cells'

proliferation, differentiation, and survival by disrupting the MAPK signaling pathway (*18*). We observed significant down-regulation of ErbB3 in LM-MEL-33– and LM-MEL-64 cell–derived EVs on day 3 ($P < 0.05$; fig. S5, B and D). After chronic drug exposure for 9 days, LM-MEL-64 cell–derived EVs showed an increase of the MCAM/MCSP expression ratio from 31.3 to 110.5% (Fig. 4D), and SK-MEL-28 cell–derived EVs from 20.7 to 82.6% (Fig. 4C). LM-MEL-28 cell–derived

Fig. 4. The anti-CD63 functionalized EPAC for monitoring phenotypic changes of EVs from melanoma patient–derived cell lines in response to BRAF inhibitor treatment. EVs released from (**A**) LM-MEL-64 cells without treatment were used as a control and followed for 30 days. EVs derived from (**B**) LM-MEL-33, (**C**) SK-MEL-28, (**D**) LM-MEL-64, and (**E**) LM-MEL-35 cell lines were collected before (day 0), during (days 3 to 30), and after treatment (days 33 and 39). (A to E) Average biomarker signals are represented by red (MCSP), blue (MCAM), green (ErbB3), and yellow (LNGFR). LM-MEL-35 cell line is BRAF wild type but NRAS mutant, and the other three cell lines are BRAF mutant. Data in (A) to (E) are represented as means ± standard deviation, where error bars represent standard deviation of three separate experiments. (**F** to **J**) Clustering of EV populations before, during, and after treatment via LDA of SERS signals.

EVs showed a significant decrease of the MCSP level on day 9 compared to day 3 ($P < 0.05$; fig. S5C). With the continuous drug treatment for 30 days, only the ErbB3 level in EVs derived from LM-MEL-33 and LM-MEL-64 cell lines showed significant down-regulation compared to EVs from their parental cell lines ($P < 0.05$; fig. S5, B and D). When the drug was removed (days 33 and 39), a strong up-regulation of MCSP and/or MCAM levels appeared in EVs derived from these two BRAF V600E mutant melanoma cell lines ($P < 0.05$; fig. S5, B and D), potentially suggesting the release from MAPK block.

Our control cell line used here, LM-MEL-35, is BRAF wild type but NRAS mutant, and is therefore susceptible to the paradoxical MAPK pathway activation by BRAF inhibition (*34*). Levels of MCSP, LNGFR, and ErbB3 did not change significantly during and after treatment ($P > 0.05$; fig. S5E). However, the MCAM level gradually increased and was significantly higher on day 39 compared with day 0 ($P < 0.05$; fig. S5E). If this observed increase is caused by enhanced MAPK signaling itself, direct cross-talk to the phosphoinositide 3-kinase (PI3K) pathway or just a correlation remains to be further explored. However, this seems to be in line with MCAM up-regulation

in the treatment-susceptible cell lines after BRAF inhibition removal and proliferation rebounce (*35*, *36*).

To comprehensively evaluate the effect of drug treatment on EV phenotypes based on the chosen biomarkers, we performed linear discriminant analysis (LDA) on the SERS data of Fig. 4 (A to E). The LDA result showed an obvious shift of BRAF V600E mutant cell–derived EV populations during and after treatment (Fig. 4, G to I), compared to the closely grouped EVs from LM-MEL-64 cells without treatment (Fig. 4F). In contrast, the drug-insensitive LM-MEL-35 cell–derived EV populations before, during, and after treatment still partially overlapped with each other (Fig. 4J), indicating minor phenotypic changes due to treatment. These LDA results further suggested the effect of BRAF inhibitor treatment on the phenotypes of EVs derived from BRAF mutant cell lines.

Drug-sensitive cells under treatment may degrade and release cell debris into their environment (*37*). These cell debris including cellular breakdown products (membranes and nucleosomes) might be detected by EPAC and thus might cause false-positive signals. Therefore, to explore the potential interferences of cell debris in characterizing EV phenotypes during drug treatment, we selected the time point of drug-treated SK-MEL-28 cells with the lowest cell viability (i.e., day 5, ~65% viability; fig. S6A), where the concentration of cell debris was expected to be the highest. The purity of EVs analyzed by EPAC was determined by an "exclusion marker"—endoplasmic reticulum protein calnexin—which is cell specific and is expected to be absent in EVs (*21*). We then analyzed the conditioned culture medium of drug-treated SK-MEL-28 cells by the anti-CD63 functionalized EPAC. The drug-treated SK-MEL-28 cell lysate was used as a positive control to mimic the cellular breakdown products during the treatment, although it is unknown whether treatment effects on cells could be recapitulated by the chemical cell lysis. The false-color SERS spectral images based on the signals of calnexin-TFMBA SERS nanotags at 1375 cm^{-1} (fig. S6B) showed the high abundance of calnexin in the cell lysate and the absence of calnexin in EVs isolated from the conditioned culture medium, indicating that EPAC results were unaffected by cellular debris and apoptotic bodies. The corresponding average SERS spectra (fig. S6C) and characteristic peak intensity measurements (fig. S6D) showed 82-fold stronger signals for calnexin in the cell lysate compared to the EVs captured from the conditioned culture medium, further suggesting that EPAC efficiently minimized the interferences from cellular debris and apoptotic bodies. These findings were further validated using Western blotting of the cell lysate and purified EVs (fig. S6E). These results provided additional evidence for demonstrating the accurate characterization of the obtained EV phenotypic evolution during the treatment.

Collectively, our results showed that our technology is capable of tracking and characterizing the phenotypic evolution of cancer cell–derived EVs during treatment with BRAF inhibitors. Here, we used four biomarkers chosen mainly due to their well-described expression in melanoma and their potential involvement in tumorigenesis. In addition, it is unknown whether CD63 or these four biomarkers are affected by oncogenic drivers or therapy in melanoma (cells and EVs), thereby affecting the assay interpretation. We envision that using biomarkers that are carefully validated in large and well-annotated patient cohorts in future will allow the successful identification of emerging drug resistance. This will hopefully aid in the prompt modification of therapeutic strategies before treatment failure.

Patient plasma EV phenotypes

The plasma EVs from 11 melanoma patients and 12 healthy individuals were detected by the anti-MCSP functionalized EPAC (Fig. 5A). Specifically, to mimic intra- and interpatient heterogeneity, we tested 15 random melanoma patient plasma samples from 11 melanoma patients (P1, P4, P7, and P9 samples are from the same patient but different time points, as are P5 and P10). Before the patient sample analysis, the specificity of the anti-MCSP functionalized EPAC was demonstrated in EVs derived from high MCSP-expressing SK-MEL-28 and low MCSP-expressing MCF7 cell lines (fig. S7). The captured EVs were subsequently detected by labeling with four-plexed SERS nanotags. We observed a strong MCSP signal for SK-MEL-28 cell–derived EVs and only a low signal for EVs from MCF7 and other control studies (i.e., EV-free cell culture medium, without the capture antibody, or nontarget CD45 detection antibodies on SERS nanotags), demonstrating the specificity of the anti-MCSP functionalized EPAC. We found that anti-MCSP captured SK-MEL-28 cell–derived EVs had different phenotypes (fig. S7C) in comparison to the anti-CD63 captured ones (Fig. 3D), likely due to the distinct EV subpopulations secreted from the SK-MEL-28 cell line. This EV heterogeneity might further reflect potential genetic or epigenetic heterogeneity in the SK-MEL-28 cell population or a differential sorting mechanism in a clonal population.

We then analyzed plasma EVs from melanoma patients and healthy controls. It is noticed that our melanoma patients' and healthy donors' samples are from different sources. However, as shown in Fig. 5A, melanoma patient samples (P1 to P15) could be differentiated from both sources of healthy controls (H1 to H5 and H6 to H12) based on the high melanoma-associated MCSP level. The representative false-color SERS spectral images (Fig. 5B) and corresponding average SERS spectra (Fig. 5C) from patient plasma samples (P1 and P8), and normal controls (H1), were given as an example, further suggesting that the unique plasma EV phenotypes of individual patients provided by the anti-MCSP functionalized EPAC enabled the successful differentiation of melanoma patients and healthy controls. Furthermore, these data suggested that EPAC could potentially shed light on the EV heterogeneity, which could help to elucidate the precise role of EV subpopulations in individual patients' pathophysiological processes, ultimately advancing the development of EVs as personalized therapeutics and diagnostics (*38*).

We validated anti-MCSP functionalized EPAC results by conventional ELISAs. Given the limited amounts of patient samples available, we strategically performed ELISA for validating the expression of MCSP and ErbB3 in EVs from melanoma patient (P1 to P10) and normal plasma (H1 to H5) samples. We found that no MCSP signals were detected, which was likely due to the insufficient ELISA sensitivity (i.e., the limit of detection = 1.23 ng/ml). For ErbB3, the ELISA results were in agreement with EPAC findings in P8, P9, and P10 plasma samples, as indicated in fig. S8. There was a result deviation between ELISA and EPAC for ErbB3 levels in P4, H3, and H5 plasma samples, which might have been caused by differences in the immunoassay formats. The conventional ErbB3 ELISA captured and labeled EVs with anti-ErbB3 antibodies, while EPAC used anti-MCSP antibodies for EV capture and anti-ErbB3 antibodies for detection. Different immunoassay formats thus might bias the assay toward a specific subset of EVs, which could explain the result differences.
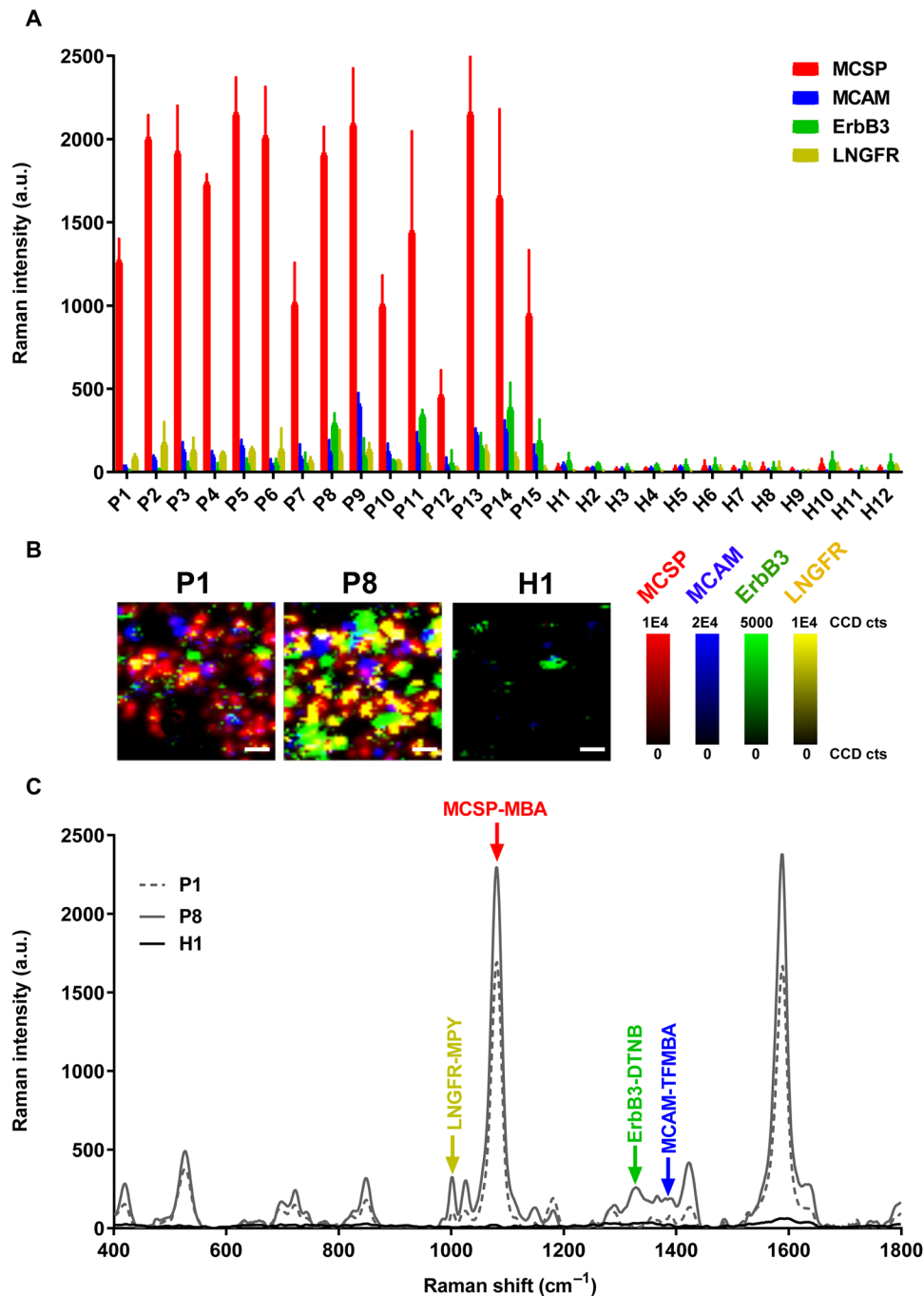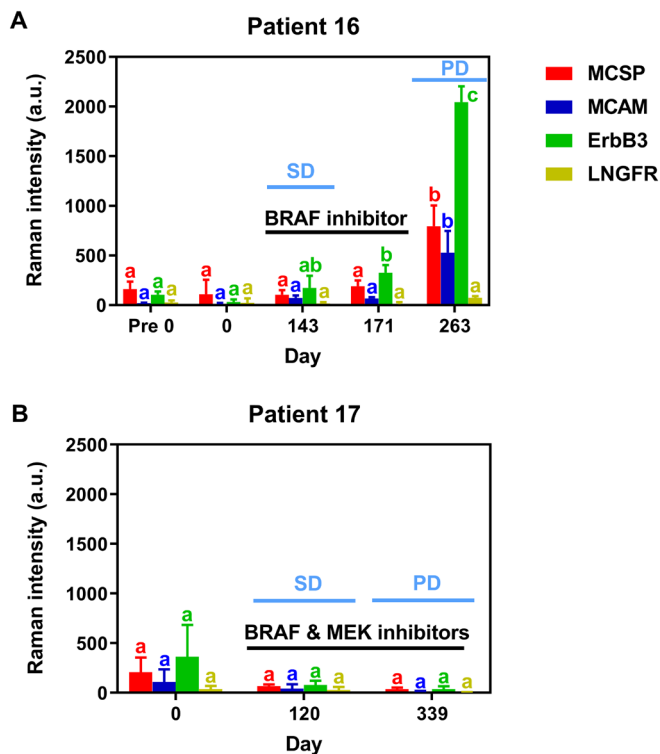
Fig. 5. The anti-MCSP functionalized EPAC for phenotyping of plasma EVs from melanoma patients. (**A**) EV phenotypes of 15 melanoma samples (P1 to P15) and 12 healthy controls (H1 to H12). P1, P4, P7, and P9 are from the same patient but different time points, as are P5 and P10. (**B**) Representative false-color SERS spectral images and (**C**) corresponding average SERS spectra from patient and normal samples (P1, P8, and H1). For (A) and (B), the biomarker signals are represented by red (MCSP), blue (MCAM), green (ErbB3), and yellow (LNGFR). Data in (A) are represented as means ± standard deviation, where error bars represent standard deviation of three separate experiments. Scale bars, 10 μm.

Monitoring the phenotypic evolution of patients' plasma EVs in response to treatment

To explore the potential applications of plasma EV phenotypes for monitoring treatment responses, we performed serial measurements of eight melanoma patients before, during, and after targeted therapies (patients 16 to 23; Fig. 6 and fig. S9) using the anti-MCSP functionalized EPAC. The patients were followed for 143 to 840 days and received intermittent to continuous BRAF inhibitor monotherapy (e.g., dabrafenib) and/or combined therapy with BRAF and MAPK/ERK kinase (MEK) inhibitors (e.g., dabrafenib and trametinib). Disease staging into progressive disease, partial response, and stable disease was made according to the radiological imaging. The SERS measurement

Fig. 6. The anti-MCSP functionalized EPAC for monitoring EV phenotypic evolution of patients 16 and 17 during targeted therapies. (**A**) Patient 16 was treated with the BRAF inhibitor monotherapy (dabrafenib). The radiological imaging test indicated that this patient showed stable disease (SD) on day 143 and developed progressive disease (PD) after cessation of treatment (day 263). (**B**) Patient 17 received the combination treatment of BRAF and MEK inhibitors (dabrafenib and trametinib). This patient showed stable disease on day 120 and progressive disease at the third visit (day 339). Data are represented as means ± standard deviation, where error bars represent standard deviation of three separate experiments. Means not sharing a common letter are significantly different ($P < 0.05$).

data of these patients were compared with healthy controls' using one-way ANOVA and summarized in table S1. Our method also enabled the monitoring of patients' EV phenotypic evolution and allowed unique insights into the plasticity of melanoma EVs during treatment. For instance, patient 16 showed the elevated ErbB3 expression on day 171 compared to day 0 ($P < 0.05$). We also observed the significant up-regulation of MCSP, MCAM, and ErbB3 on day 263, which was consistent to the phenomenon that we observed in EVs derived from BRAF inhibitor–treated BRAF mutant melanoma cells after release from drug treatment and rebound in cellular proliferation (Fig. 4 and fig. S5). Nevertheless, any correlation between EV phenotype and clinical data is mere speculation at this stage.

Patient 17 received combination treatment with BRAF and MEK inhibitors (Fig. 6B). Before treatment, this patient showed significantly higher expressions of MCSP, MCAM, and ErbB3 compared to the mean values of healthy controls (table S1). During treatment, this patient showed low expressions of all four target biomarkers, whose radiological imaging indicated stable disease on day 120 and progressive disease on day 339. This demonstrates that, while the described technology has exciting potential and allows sensitive multiplex biomarker-based EV tracking, the choice of biomarkers

(and the number of biomarkers to be monitored) will be critical for clinical translation.

In conclusion, monitoring patient responses is important to guide treatment management and improve the clinical outcome. Here, we proposed to monitor patient treatment responses based on plasma EV phenotypes using EPAC. EPAC integrates a nanomixing-enhanced EV microchip and a multiplex SERS signal readout system to enable a comprehensive investigation of low-abundance tumor-specific EVs present in complex biological fluids, without the need for EV purification and enrichment steps. The reliability of EPAC was evaluated carefully and demonstrated to precisely profile the EV phenotypic evolution during treatment. By tracking the EV phenotypic changes, we were able to infer the treatment response and obtain tumor cell–specific information. The successful identification of melanoma patient plasma EV phenotypes with high sensitivity further demonstrated the potential of EPAC for routine EV analysis in the clinic. We also observed changes in plasma EV phenotypes during treatment in eight melanoma patients receiving molecular-targeted therapies. The biomarker combination chosen here was used to demonstrate the potential of the technology but not specifically designed or validated to allow the identification of specific treatment responses to BRAF inhibition. As we only used four biomarkers of known value in tracking melanoma (*17*), it seems feasible that—with biomarker panels specifically targeted for cancer types and treatments and given the streamlined features of EPAC—our method has great potential to guide personalized cancer medicine.

MATERIALS AND METHODS
Clinical sample acquisition
This study was conducted according to the National Health and Medical Research Council (NHMRC) Australian Code for the responsible conduct of Research and the National Statement on Ethical Conduct in Human Research. Patients and healthy donors (H6 to H12) have provided their written informed consent for the research study protocol, which were approved by the Human Research Ethics Committee of the Austin Hospital (Melbourne) and Princess Alexandra Hospital (Brisbane), respectively. Ethics approvals were obtained from The University of Queensland Institutional Human Research Ethics Committee (approval nos. 2011001315 and 2016000876). Healthy donors' blood samples (H1 to H5) were obtained from Red Cross blood. All blood samples were processed using the same standard protocol in accordance with approved guidelines. The demographic data for all patients and healthy donors have been summarized in table S2.

Cell culture
Three melanoma cell lines—LM-MEL-33, LM-MEL-35, and LM-MEL-64—were established at the Ludwig Institute for Cancer Research in Melbourne from patient tumor samples. SK-MEL-28 and MCF7 were obtained from the American Type Culture Collection. All cell lines were authenticated by short-tandem repeat profiling (CellBank Australia) and cultured for <6 months after authentication. Cells were maintained in RF10 medium, which is made up of RPMI 1640 medium (Gibco), 10% fetal bovine serum (Gibco), 2 mM GlutaMAX (Gibco), and 1% penicillin-streptomycin (Gibco), and kept in a humidified incubator in 5% CO_2 at 37°C. All cell lines were routinely tested for mycoplasma.

Preparation of conditioned culture medium

In the sensitivity and specificity assays, SK-MEL-28 and MCF7 cell lines were maintained in serum-free medium for 48 hours to generate conditioned culture medium. In the study of investigating drug effects on EV phenotypes, SK-MEL-28, LM-MEL-33, LM-MEL-35, and LM-MEL-64 cell lines were maintained in Medium 254 (Gibco) with Human Melanocyte Growth Supplement, and with/without 1 μM PLX4720 (Selleckchem), whose conditioned culture media were collected every 3 days. To remove detached cells and cellular debris, conditioned culture media were centrifuged at 800*g* for 10 min. The cell-free supernatant was then stored at −80°C for the following experiments.

Proliferation assays

Cellular viability was assessed using the CellTiter 96 AQueous One Solution Cell Proliferation Assay (Promega Corporation, Madison, WI) according to the manufacturer's protocol.

Flow cytometry

The collected cells were first labeled with either mouse anti-human MCSP (R&D Systems, MAB2585), MCAM (R&D Systems, MAB932), ErbB3 (R&D Systems, MAB3481), LNGFR (R&D Systems, MAB367) monoclonal antibodies, or isotype-matched control [normal mouse immunoglobulin G (IgG), sc-2025, Santa Cruz Biotechnology], followed by Alexa Fluor 488–labeled goat anti-mouse IgG (H+L) secondary antibodies. The flow cytometry measurements were performed with BD Accuri C6, and the data were analyzed with FlowJo (TreeStar, Ashland, OR).

EV preparation for Western blot analysis

EVs were isolated by the combination of ultrafiltration (Amicon Ultra-15 Centrifugal Filter Device, Merck) and Total Exosome Isolation Kit (Life Technologies Australia Pty Ltd.), according to manufacturers' instructions. Briefly, conditioned culture media were centrifuged at 2000*g* for 30 min to further remove cells and debris. The 12 ml of resulting conditioned culture media was then transferred to an Ultra-15 50-kDa device and concentrated to 120 μl using an Allegra X-22R centrifuge at 4000*g* for 20 min at 4°C. The concentrate was transferred to a new tube and mixed with 60 μl of Total Exosome Isolation reagent by vortexing. The concentrate/reagent mixture was incubated overnight at 4°C and subsequently centrifuged at 10,000*g* for 1 hour at 4°C. The supernatants were discarded, and EVs were contained in the pellet at the bottom of the tube.

Western blot analysis

The collected EVs were lysed in Pierce immunoprecipitation lysis buffer containing 1× protein inhibitor (Roche) and 1 mM phenylmethylsulfonyl fluoride (Thermo Fisher Scientific), and the protein concentration was quantified using the bicinchoninic acid assay (BCA assay; Thermo Fisher Scientific). Protein lysates were resolved by SDS–polyacrylamide gel electrophoresis and transferred onto polyvinylidene difluoride (PVDF) membranes (Invitrogen). The PVDF membrane was blocked with 5% nonfat dry milk in tris-buffered saline buffer for 1 hour at room temperature (RT) and then immunoblotted with 500-fold diluted primary antibodies overnight at 4°C. The primary antibodies used in this study included mouse anti-human MCSP (R&D Systems, MAB2585), MCAM (R&D Systems, MAB932), ErbB3 (R&D Systems, MAB3482), LNGFR (R&D

Systems, MAB367; or Santa Cruz Biotechnology, sc-271708), calnexin (Abcam, ab112995), and CD63 (Novus, NBP2-42225). Proteins were analyzed under denaturing and reducing/nonreducing conditions according to the manufacturer's instructions. After incubation, the PVDF membrane was washed with phosphate-buffered saline (PBS) containing 0.1% Tween 20 and then incubated with IRDye 800CW–conjugated goat anti-mouse (LI-COR, 926-32210, 10,000-fold dilution) for 1 hour at RT. After washing, protein bands were detected using the Odyssey LI-COR CLx Imaging System.

Size exclusion purification

Five hundred microliters of processed plasma (centrifuged at 10,000*g* for 10 min) was overlaid on size exclusion columns filled with Sepharose 4B resins (Sigma Aldrich, Australia) and followed by elution with PBS. The fractions were then collected to determine the particle and protein concentrations via the Micro BCA assay. High particle/low protein fractions were pooled and concentrated in an Amicon Ultra-2 50-kDa centrifugal filter device for the ELISA assay.

Enzyme-linked immunosorbent assay

The expressions of MCSP and ErbB3 on the surface of EVs were measured using commercial ELISA kits: MCSP (Sigma-Aldrich, RAB1594) and ErbB3 (Sigma-Aldrich, RAB0174). The assays were conducted according to the manufacturer's instructions. Briefly, 100 μl of standards, controls, and unknown samples was introduced to selected wells and incubated at 4°C overnight. Afterward, the reaction wells were washed four times with wash buffer. One hundred microliters of biotinylated detection antibody was then added to all wells and incubated for 1 hour at RT with gentle shaking. The wells were subsequently washed four times with wash buffer. The horseradish peroxidase–streptavidin reagent was added to all wells and incubated for 45 min at RT. The reaction wells were then washed four times with wash buffer, followed by 30-min incubation with 100 μl of 3,3′,5,5′-tetramethylbenzidine reagent at RT in the dark with gentle shaking. Last, all wells were supplemented with 50 μl of stop solution and analyzed for absorbance at 450 nm.

Nanoparticle tracking analysis

The concentrations and particle size distributions of EVs present in conditioned culture medium were analyzed using NanoSight N300 (Malvern Panalytical, UK), based on their properties of both light scattering and Brownian motion. For each sample, three videos of 60-s duration were recorded, with a short delay between recordings. The recorded video was analyzed with NTA software, which tracked many particles individually and, using the Stokes-Einstein equation, calculated their hydrodynamic diameters. Camera sensitivity and detection threshold were set to 12 and 5, respectively. The concentration of each detection sample was between 2×10^8 and 6×10^8 particles/ml, which was prepared by 10-fold dilution of the stock conditioned culture medium with PBS that has passed through a 0.22-μm filter. Samples were administered and recorded under controlled flow, using the NanoSight syringe pump and script control system.

SERS nanotag synthesis

SERS nanotags were prepared by functionalizing AuNPs with antibodies and Raman reporters and stabilizing with bovine serum albumin (BSA; Life Technologies Australia Pty Ltd.) coatings. Briefly, 60-nm AuNPs were synthesized by citrate reduction of $HAuCl_4$

(39). Ten microliters of 1 mM Raman reporters in ethanol (either MBA, TFMBA, DTNB, or MPY) and subsequently 2 µl of 1 mM dithiobis(succinimidyl propionate) (Thermo Fisher Scientific) in dimethyl sulfoxide were added into 1 ml of AuNP solutions and incubated for 5 hours at RT to form a complete self-assembled monolayer. For the functionalization of MPY Raman reporters, 20 µl of 0.1 M NaOH was first added to adjust AuNP solutions to pH = 8. After incubation, the mixture was centrifuged at 7600 rpm for 10 min to remove the residual reactants. The mixture was then resuspended in 200 µl of 0.1 mM PBS and incubated with 2 µg of primary antibodies against either MCSP (R&D Systems, MAB2585), MCAM (R&D Systems, MAB932), ErbB3 (R&D Systems, MAB3481), LNGFR (R&D Systems, MAB367), calnexin (Abcam, ab112995), or CD45 (BioLegend, 368502) for 30 min at RT. The mixture was then centrifuged at 600g at 4°C for 10 min to remove free antibodies and resuspended in 200 µl of 0.1% (w/v) BSA for 0.5 hour at RT to block nonspecific binding sites and stabilize SERS nanotags. The SERS nanotags were stored at 4°C and were stable for months.

Microchip fabrication
The device was fabricated using standard photolithography and soft lithography according to the procedure reported previously (20). Briefly, the device was assembled from a glass chip with patterned asymmetric gold electrode structures and a polydimethylsiloxane (PDMS) slab consisting of the microfluidic channel structures. The PDMS slab consisted of five parallel channels, each 3.5 cm long, 400 µm wide, and 500 µm high. The chip accommodated five channels, and each channel was made up of an array of 40 pairs of asymmetric gold electrodes (fig. S1, A and B). The distance between two adjacent electrode pairs was 150 µm. An electrode pair consisted of a small (100 µm width) and large (400 µm width) electrodes that were spaced by a distance of 50 µm (fig. S1C). The nanoscopic fluid flow was generated by applying an alternating potential difference across each asymmetric electrode pair. The potential difference changed the charge distribution in the electrical double layer that gave rise to a lateral fluid movement in nanometer distance to the electrode surface. This lateral fluid movement increased the diffusion of molecules and SERS nanotags, leading to frequent antigen-antibody collisions while simultaneously shearing off weakly bound nonspecific molecules.

The electrode structures were designed in L-Edit (Tanner Research, USA) and written to a 12.7 cm chrome mask (Shenzhen Qingyi Precision Mask Making, Singapore) using a direct laser writer (Heidelberg µPG 101, Germany). Borofloat wafers (Bonda Technology Pte Ltd., Singapore) were rinsed with isopropanol and acetone and dried for 25 min at 150°C. Subsequently, negative photoresist AZ nLOF 2020 (MicroChemicals GmbH, Germany) was spin-coated on the wafer for 30 s at 3000 rpm before a soft bake for 2 min at 110°C. Next, the coated wafer was exposed at a constant dose of 340 mJ/cm with an EVG 620 mask aligner (EV Group, Austria), followed by a postback of 1 min at 110°C. The exposed wafer was then developed for 45 s in AZ 726 MIF (MicroChemicals GmbH, Germany), dried, and subjected to deposition of 10 nm of Ti and 200 nm of Au with a Temescal FC-2000 electron beam evaporator (Ferrotec, USA). After overnight liftoff in Remover PG (MicroChemicals GmbH, Germany), the excess material was washed off and the electrode pattern was revealed (fig. S1B).

PDMS microfluidic channels were prepared by casting an activated silicon elastomer solution (Sylgard 184, Dow, USA) onto the master mold containing microfluidic channels. After curing for 20 min at 80°C, the PDMS was carefully detached from the master. The sample inlet and outlet reservoirs were then punched at the ends of microfluidic channels. The PDMS microfluidic structures were aligned with the array of asymmetric electrodes on the glass chip and thermally bonded overnight at 65°C.

Microchip functionalization
The device was functionalized in a three-step procedure using biotin-avidin chemistry (fig. S1D). Initially, the device channels were washed with PBS buffer. Next, the channels were sequentially incubated with solutions of biotinylated BSA (200 µg/ml) for 2 hours, streptavidin (100 µg/ml) for 1 hour, biotinylated anti-human CD63 antibody (10 µg/ml) (BioLegend, 353018) or biotinylated anti-human MCSP antibody (10 µg/ml) (MACS Miltenyi Biotec, 130-099-049) for 2 hours, and 1% (w/v) BSA for 0.5 hour at RT. After each incubation step, the channels were washed with PBS buffer to remove excess reagents.

EV capture and labeling
One hundred microliters of samples (i.e., conditioned culture medium or 10-fold diluted plasma) and 30 µl of diluted SERS nanotags were subsequently run in each microfluidic channel for 40 min under the field condition of 100 mV and 1 kHz. Under these previously optimized conditions (20), the stimulated nanoscopic fluid flow was the most efficient for EV capture and labeling due to the increased collision frequency of EVs with capture antibodies and SERS nanotags, and the minimum nonspecific binding.

SERS measurements
SERS mapping was performed using a WITec Alpha300 R microspectrometer configured with a 632-nm laser and a highly sensitive electron multiplying charge-coupled device (EMCCD). The laser power of 4 mW and the system frequency were calibrated by the peak of a silicon wafer at ~520 cm^{-1}. SERS mapping was performed at an area of 60 µm × 60 µm (60 pixels × 60 pixels) with 1-µm spatial resolution using a 20× microscope objective. The SERS spectrum from each pixel was generated with 50-ms integration time. The sample was measured in triplicate; for each replicate, three different positions (left, middle, and right) across the entire channel were scanned. The selected region was scanned to simultaneously detect all four biomarkers, and average SERS spectra were calculated from these spectral images.

Atomic force microscopy
EVs captured on the electrode surface were in situ characterized using a Cypher AFM system (Asylum Research, USA) on air tapping mode with cantilevers (HA_NC, ETALON, TipsNano, Russia) with a resonant frequency of 140 kHz (dispersion ±10%), a force constant of 3.5 N/m (dispersion ±20%), and a <10-nm curvature radius sharp silicon tip.

Statistical analyses
Data were presented as means ± standard deviation. One-way ANOVA followed by either Tukey's or Dunnett's multiple comparisons test was performed to identify significant variations at 95% confidence interval, using GraphPad Prism 7.0 (GraphPad Software Inc., USA).

To statistically investigate the EV phenotypic changes in response to treatment, SERS intensities at peaks of 1075, 1375, 1335,

and 1000 cm^{-1}—representing the expression of each biomarker—were used as LDA input variables. LDA then generated discriminant functions that consisted of different linear combinations of input variables. The resulting discriminant functions were uncorrelated with each other, and each function maximized the difference between groups on that function. The first two discriminant functions that explained most input variables were selected for EV phenotypic clustering. Discriminant scores generated from these two discriminant functions were plotted to describe the differences between each data point. LDA was performed with SPSS 19.0 software package (SPSS Inc., USA).

SUPPLEMENTARY MATERIALS
Supplementary material for this article is available at http://advances.sciencemag.org/cgi/content/full/6/9/eaax3223/DC1

Fig. S1. EPAC design and functionalization.
Fig. S2. EPAC-captured EV characterization.
Fig. S3. Western blot analysis of isolated EVs from SK-MEL-28 and MCF7 cells.
Fig. S4. Performance evaluation of the anti-CD63, anti-CD9, or anti-CD81 functionalized EPAC for detection of MCSP-positive EVs from SK-MEL-28 cells.
Fig. S5. Monitoring the changes of individual biomarker levels in EVs from drug-treated melanoma cell lines, using the anti-CD63 functionalized EPAC.
Fig. S6. Effect of cell debris on the anti-CD63 functionalized EPAC performance.
Fig. S7. Anti-MCSP functionalized EPAC specificity.
Fig. S8. The ErbB3 expression in EVs derived from melanoma patient (P1 to P10) and normal plasma (H1 to H5) samples, measured with a commercial ELISA kit.
Fig. S9. The anti-MCSP functionalized EPAC for tracking EV phenotypic changes of patients 18 to 23 during targeted therapies.
Table S1. The anti-MCSP functionalized EPAC for measurements of plasma EVs from 12 healthy donors (H1 to H12) and 8 melanoma patients (P16 to P23).
Table S2. Demographic data for melanoma patients and healthy donors.

View/request a protocol for this paper from *Bio-protocol*.

REFERENCES AND NOTES
1. E. V. Abel, K. J. Basile, C. H. Kugel III, A. K. Witkiewicz, K. Le, R. K. Amaravadi, G. C. Karakousis, X. Xu, W. Xu, L. M. Schuchter, J. B. Lee, A. Ertel, P. Fortina, A. E. Aplin, Melanoma adapts to RAF/MEK inhibitors by FOXD3-dependent upregulation of *ERBB3*. *J. Clin. Invest.* **123**, 2155–2168 (2013).
2. A. Toss, Z. Mu, S. Fernandez, M. Cristofanilli, CTC enumeration and characterization: Moving toward personalized medicine. *Ann. Transl. Med.* **2**, 108 (2014).
3. G. Raposo, W. Stoorvogel, Extracellular vesicles: Exosomes, microvesicles, and friends. *J. Cell Biol.* **200**, 373–383 (2013).
4. R. E. Lane, D. Korbie, M. M. Hill, M. Trau, Extracellular vesicles as circulating cancer biomarkers: Opportunities and challenges. *Clin. Transl. Med.* **7**, 14 (2018).
5. S. Fais, L. O'Driscoll, F. E. Borras, E. Buzas, G. Camussi, F. Cappello, J. Carvalho, A. Cordeiro da Silva, H. D. Portillo, S. E. Andaloussi, T. F. Trček, R. Furlan, A. Hendrix, I. Gursel, V. Kralj-Iglic, B. Kaeffer, M. Kosanovic, M. E. Lekka, G. Lipps, M. Logozzi, A. Marcilla, M. Sammar, A. Llorente, I. Nazarenko, C. Oliveira, G. Pocsfalvi, L. Rajendran, G. Raposo, E. Rohde, P. Siljander, G. van Niel, M. H. Vasconcelos, M. Yáñez-Mó, M. L. Yliperttula, N. Zarovni, A. B. Zavec, B. Giebel, Evidence-based clinical use of nanoscale extracellular vesicles in nanomedicine. *ACS Nano* **10**, 3886–3899 (2016).
6. K. Al-Nedawi, B. Meehan, J. Micallef, V. Lhotak, L. May, A. Guha, J. Rak, Intercellular transfer of the oncogenic receptor EGFRvIII by microvesicles derived from tumour cells. *Nat. Cell Biol.* **10**, 619–624 (2008).
7. H. Peinado, M. Alečković, S. Lavotshkin, I. Matei, B. Costa-Silva, G. Moreno-Bueno, M. Hergueta-Redondo, C. Williams, G. García-Santos, C. M. Ghajar, A. Nitadori-Hoshino, C. Hoffman, K. Badal, B. A. Garcia, M. K. Callahan, J. Yuan, V. R. Martins, J. Skog, R. N. Kaplan, M. S. Brady, J. D. Wolchok, P. B. Chapman, Y. Kang, J. Bromberg, D. Lyden, Melanoma exosomes educate bone marrow progenitor cells toward a pro-metastatic phenotype through MET. *Nat. Med.* **18**, 883–891 (2012).
8. H. Shao, J. Chung, L. Balaj, A. Charest, D. D. Bigner, B. S. Carter, F. H. Hochberg, X. O. Breakefield, R. Weissleder, H. Lee, Protein typing of circulating microvesicles allows real-time monitoring of glioblastoma therapy. *Nat. Med.* **18**, 1835–1840 (2012).
9. H. Shao, J. Chung, K. Lee, L. Balaj, C. Min, B. S. Carter, F. H. Hochberg, X. O. Breakefield, H. Lee, R. Weissleder, Chip-based analysis of exosomal mRNA mediating drug resistance in glioblastoma. *Nat. Commun.* **6**, 6999 (2015).
10. Y. Chen, L. Wang, Y. Zhu, Z. Chen, X. Qi, L. Jin, J. Jin, D. Hua, X. Ma, Breast cancer resistance protein (BCRP)-containing circulating microvesicles contribute to chemoresistance in breast cancer. *Oncol. Lett.* **10**, 3742–3748 (2015).
11. X. Ma, Z. Chen, D. Hua, D. He, L. Wang, P. Zhang, J. Wang, Y. Cai, C. Gao, X. Zhang, F. Zhang, T. Wang, T. Hong, L. Jin, X. Qi, S. Chen, X. Gu, D. Yang, Q. Pan, Y. Zhu, Y. Chen, D. Chen, L. Jiang, X. Han, Y. Zhang, J. Jin, X. Yao, Essential role for TrpC5-containing extracellular vesicles in breast cancer with chemotherapeutic resistance. *Proc. Natl. Acad. Sci. U.S.A.* **111**, 6389–6394 (2014).
12. K. Liang, F. Liu, J. Fan, D. Sun, C. Liu, C. J. Lyon, D. W. Bernard, Y. Li, K. Yokoi, M. H. Katz, E. J. Koay, Z. Zhao, Y. Hu, Nanoplasmonic quantification of tumour-derived extracellular vesicles in plasma microsamples for diagnosis and treatment monitoring. *Nat. Biomed. Eng.* **1**, 0021 (2017).
13. Y. Yoshioka, N. Kosaka, Y. Konishi, H. Ohta, H. Okamoto, H. Sonoda, R. Nonaka, H. Yamamoto, H. Ishii, M. Mori, K. Furuta, T. Nakajima, H. Hayashi, H. Sugisaki, H. Higashimoto, T. Kato, F. Takeshita, T. Ochiya, Ultra-sensitive liquid biopsy of circulating extracellular vesicles using ExoScreen. *Nat. Commun.* **5**, 3591 (2014).
14. E. A. Kwizera, R. O'Connor, V. Vinduska, M. Williams, E. R. Butch, S. E. Snyder, X. Chen, X. Huang, Molecular detection and analysis of exosomes using surface-enhanced Raman scattering gold nanorods and a miniaturized device. *Theranostics* **8**, 2722–2738 (2018).
15. H. Im, H. Shao, Y. I. Park, V. M. Peterson, C. M. Castro, R. Weissleder, H. Lee, Label-free detection and molecular profiling of exosomes with a nano-plasmonic sensor. *Nat. Biotechnol.* **32**, 490–495 (2014).
16. H. Davies, G. R. Bignell, C. Cox, P. Stephens, S. Edkins, S. Clegg, J. Teague, H. Woffendin, M. J. Garnett, W. Bottomley, N. Davis, E. Dicks, R. Ewing, Y. Floyd, K. Gray, S. Hall, R. Hawes, J. Hughes, V. Kosmidou, A. Menzies, C. Mould, A. Parker, C. Stevens, S. Watt, S. Hooper, R. Wilson, H. Jayatilake, B. A. Gusterson, C. Cooper, J. Shipley, D. Hargrave, K. Pritchard-Jones, N. Maitland, G. Chenevix-Trench, G. J. Riggins, D. D. Bigner, G. Palmieri, A. Cossu, A. Flanagan, A. Nicholson, J. W. C. Ho, S. Y. Leung, S. T. Yuen, B. L. Weber, H. F. Seigler, T. L. Darrow, H. Paterson, R. Marais, C. J. Marshall, R. Wooster, M. R. Stratton, P. A. Futreal, Mutations of the *BRAF* gene in human cancer. *Nature* **417**, 949–954 (2002).
17. S. C.-H. Tsao, J. Wang, Y. Wang, A. Behren, J. Cebon, M. Trau, Characterising the phenotypic evolution of circulating tumour cells during treatment. *Nat. Commun.* **9**, 1482 (2018).
18. E. R. Cantwell-Dorris, J. J. O'Leary, O. M. Sheils, BRAF^{V600E}: Implications for carcinogenesis and molecular therapy. *Mol. Cancer Ther.* **10**, 385–394 (2011).
19. Y. Wang, R. Vaidyanathan, M. J. A. Shiddiky, M. Trau, Enabling rapid and specific surface-enhanced Raman scattering immunoassay using nanoscaled surface shear forces. *ACS Nano* **9**, 6354–6362 (2015).
20. R. Vaidyanathan, M. Naghibosadat, S. Rauf, D. Korbie, L. G. Carrascosa, M. J. A. Shiddiky, M. Trau, Detecting exosomes specifically: A multiplexed device based on alternating current electrohydrodynamic induced *nanoshearing*. *Anal. Chem.* **86**, 11125–11132 (2014).
21. R. J. Lobb, M. Becker, S. W. Wen, C. S. F. Wong, A. P. Wiegmans, A. Leimgruber, A. Möller, Optimized exosome isolation protocol for cell culture supernatant and human plasma. *J. Extracell. Vesicles* **4**, 27031 (2015).
22. F. A. W. Coumans, E. L. Gool, R. Nieuwland, Bulk immunoassays for analysis of extracellular vesicles. *Platelets* **28**, 242–248 (2017).
23. N. Koliha, U. Heider, T. Ozimkowski, M. Wiemann, A. Bosio, S. Wild, Melanoma affects the composition of blood cell-derived extracellular vesicles. *Front. Immunol.* **7**, 282 (2016).
24. P. Sharma, S. Ludwig, L. Muller, C. S. Hong, J. M. Kirkwood, S. Ferrone, T. L. Whiteside, Immunoaffinity-based isolation of melanoma cell-derived exosomes from plasma of patients with melanoma. *J. Extracell. Vesicles* **7**, 1435138 (2018).
25. J. de Vrij, S. L. N. Maas, M. van Nispen, M. Sena-Esteves, R. W. A. Limpens, A. J. Koster, S. Leenstra, M. L. Lamfers, M. L. D. Broekman, Quantification of nanosized extracellular membrane vesicles with scanning ion occlusion sensing. *Nanomedicine* **8**, 1443–1458 (2013).
26. E. S. Gray, A. L. Reid, S. Bowyer, L. Calapre, K. Siew, R. Pearce, L. Cowell, M. H. Frank, M. Millward, M. Ziman, Circulating melanoma cell subpopulations: Their heterogeneity and differential responses to treatment. *J. Invest. Dermatol.* **135**, 2040–2048 (2015).
27. Q. Zeng, W. Li, D. Lu, Z. Wu, H. Duan, Y. Luo, J. Feng, D. Yang, L. Fu, X. Yan, CD146, an epithelial-mesenchymal transition inducer, is associated with triple-negative breast cancer. *Proc. Natl. Acad. Sci. U.S.A.* **109**, 1127–1132 (2012).
28. X. Wang, T. Osada, Y. Wang, L. Yu, K. Sakakura, A. Katayama, J. B. Mc Carthy, A. Brufsky, M. Chivukula, T. Khoury, D. S. Hsu, W. T. Barry, H. K. Lyerly, T. M. Clay, S. Ferrone, CSPG4 protein as a new target for the antibody-based immunotherapy of triple-negative breast cancer. *J. Natl. Cancer Inst.* **102**, 1496–1512 (2010).
29. Z. Aguilar, R. W. Akita, R. S. Finn, B. L. Ramos, M. D. Pegram, F. F. Kabbinavar, R. J. Pietras, P. Pisacane, M. X. Sliwkowski, D. J. Slamon, Biologic effects of heregulin/neu differentiation factor on normal and malignant human breast and ovarian epithelial cells. *Oncogene* **18**, 6050–6062 (1999).

30. T. N. Alver, T. J. Lavelle, A. S. Longva, G. F. Øy, E. Hovig, S. L. Bøe, MITF depletion elevates expression levels of ERBB3 receptor and its cognate ligand NRG1-beta in melanoma. *Oncotarget* **7**, 55128–55140 (2016).

31. J. Kim, R. Villadsen, T. Sørlie, L. Fogh, S. Z. Grønlund, A. J. Fridriksdottir, I. Kuhn, F. Rank, V. T. Wielenga, H. Solvang, P. A. W. Edwards, A.-L. Børresen-Dale, L. Rønnov-Jessen, M. J. Bissell, O. W. Petersen, Tumor initiating but differentiated luminal-like breast cancer cells are highly invasive in the absence of basal-like activity. *Proc. Natl. Acad. Sci. U.S.A.* **109**, 6124–6129 (2012).

32. A. Behren, M. Anaka, P.-H. Lo, L. J. Vella, I. D. Davis, J. Catimel, T. Cardwell, C. Gedye, C. Hudson, R. Stan, J. Cebon, The Ludwig institute for cancer research Melbourne melanoma cell line panel. *Pigment Cell Melanoma Res.* **26**, 597–600 (2013).

33. V. De Giorgi, P. Pinzani, F. Salvianti, M. Grazzini, C. Orlando, M. Santucci, T. Lotti, M. Pazzagli, D. Massi, Circulating tumor cells in cutaneous melanoma. *J. Invest. Dermatol.* **131**, 1776–1777 (2011).

34. G. T. Gibney, J. L. Messina, I. V. Fedorenko, V. K. Sondak, K. S. M. Smalley, Paradoxical oncogenesis—The long-term effects of BRAF inhibition in melanoma. *Nat. Rev. Clin. Oncol.* **10**, 390–399 (2013).

35. L. Tentori, P. M. Lacal, G. Graziani, Challenging resistance mechanisms to therapies for metastatic melanoma. *Trends Pharmacol. Sci.* **34**, 656–666 (2013).

36. D. B. Johnson, J. A. Sosman, Update on the targeted therapy of melanoma. *Curr. Treat. Options Oncol.* **14**, 280–292 (2013).

37. M. L. Sulciner, C. N. Serhan, M. M. Gilligan, D. K. Mudge, J. Chang, A. Gartung, K. A. Lehner, D. R. Bielenberg, B. Schmidt, J. Dalli, E. R. Greene, Y. Gus-Brautbar, J. Piwowarski, T. Mammoto, D. Zurakowski, M. Perretti, V. P. Sukhatme, A. Kaipainen, M. W. Kieran, S. Huang, D. Panigrahy, Resolvins suppress tumor growth and enhance cancer therapy. *J. Exp. Med.* **215**, 115–140 (2017).

38. E. Willms, C. Cabañas, I. Mäger, M. J. A. Wood, P. Vader, Extracellular vesicle heterogeneity: Subpopulations, isolation techniques, and diverse functions in cancer progression. *Front. Immunol.* **9**, 738 (2018).

39. G. Frens, Controlled nucleation for the regulation of the particle size in monodisperse gold suspensions. *Nature* **241**, 20–22 (1973).

Author/s:
Wang, J; Wuethrich, A; Ibn Sina, AA; Lane, RE; Lin, LL; Wang, Y; Cebon, J; Behren, A; Trau, M

Title:
Tracking extracellular vesicle phenotypic changes enables treatment monitoring in melanoma

Date:
2020-02-01

Citation:
Wang, J., Wuethrich, A., Ibn Sina, A. A., Lane, R. E., Lin, L. L., Wang, Y., Cebon, J., Behren, A. & Trau, M. (2020). Tracking extracellular vesicle phenotypic changes enables treatment monitoring in melanoma. SCIENCE ADVANCES, 6 (9), https://doi.org/10.1126/sciadv.aax3223.

Persistent Link:
http://hdl.handle.net/11343/272252

File Description:
Published version
License:
CC BY-NC